Available online at www.sciencedirect.com
ScienceDirect
Trans. Nonferrous Met. Soc. China 28(2018) 1735−1744
Transactions of Nonferrous Metals Society of China
www.tnmsc.cn

Phase precipitation behavior and tensile properties of as-cast Ni-based superalloy during heat treatment

Shuang GAO[1,2], Jie-shan HOU[1], Yong-an GUO[1], Lan-zhang ZHOU[1]

1. Institute of Metal Research, Chinese Academy of Sciences, Shenyang 110016, China;
2. University of Chinese Academy of Sciences, Beijing 100049, China

Received 10 May 2017; accepted 27 November 2017

Abstract: The phase precipitation behavior and tensile properties of an as-cast Ni-based alloy, IN617B alloy, after solution heat treatment and long-term aging treatment were investigated. Ti(C,N), M_6C and $M_{23}C_6$ are the primary precipitates in as-cast microstructure. After solution heat treatment, most of carbides dissolve into the matrix except a few fine Ti(C,N) within grains. During long-term aging at 700 °C, the phase precipitation behaviors of the alloy are characterized as follows: (1) $M_{23}C_6$ carbides at grain boundaries (GBs) transform from film-like shape to cellular shape and gradually coarsen due to the decrease of the surface energy and element aggregation to GBs; (2) $M_{23}C_6$ carbides within grains have a bar-like morphology with a preferential growth direction [110] and have a cube-on-cube coherent orientation relationship with the matrix γ; (3) γ' particles inhibit the coarsening of $M_{23}C_6$ within grains by constraining the diffusion of formation elements. Furthermore, the tensile strength of the alloy obviously increases, but the ductility significantly decreases after the aging for 5000 h. The alloy has a relatively stable microstructure which guarantees the excellent tensile properties during long-term aging.
Key words: Ni-based superalloy; phase precipitation; carbide; γ' phase; tensile properties

1 Introduction

At the beginning of the twenty-first century, there is a strong incentive to increase the working temperature and steam pressure in coal-fired power plants in order to improve plants efficiency and reduce emissions in the whole world [1,2]. Extensive attention is drawn to A-USC power generation technology which requires the work condition at 700 °C or higher and under 35 MPa. Therefore, traditional materials such as ferritic/martensitic steel, which are designed to operate at service temperature of 600 °C and steam pressure of 25 MPa, will not satisfy the requirements [2,3]. Instead, Ni-based superalloys can meet the A-USC requirements and have been investigated in detail in Europe, Japan and the United States. IN617B alloy is one of the principal candidate materials due to its excellent high-temperature strength, remarkable creep resistance, outstanding oxidation resistance and higher corrosion resistance [4,5]. IN617B alloy is a solid−solution strengthening Ni-based superalloy which mainly contains some strengthening elements such as cobalt and molybdenum. And the presence of γ' and carbides in the long-term service conditions also provides additional strength for IN617B alloy [6].

Considerable studies have been carried out on the microstructures and properties of IN617B alloy while most researches focus on wrought IN617B alloy [7−9]. In addition, the application of cast alternatives to wrought IN617B alloy is also in the plan for larger and more complex components in A-USC turbine [10]. However, few studies about cast IN617B alloy are reported at present. Many researches [11−14] on the microstructure of wrought IN617B alloy found that primary precipitates are Ti(C,N), M_6C, $M_{23}C_6$ and γ'. And they did not observe that detrimental topological closed packed phases (TCP) precipitated during long-term thermal exposure (at 482 to 871 °C for approximately 65000 h). WU et al [14] suggested that the long-term thermal stability of IN617B alloy was reasonably good over a wide temperature range of 538 to 704 °C,

Foundation item: Project (51571191) supported by the National Natural Science Foundation of China; Project (NY 20150102) supported by the National Energy Administration Program of China
Corresponding author: Jie-shan HOU; Tel: +86-24-83978469; E-mail: jshou@imr.ac.cn
DOI: 10.1016/S1003-6326(18)64817-4

whereas at higher temperatures (871 °C), the substantial decrease in the volume fraction of γ' and coarsening and clustering of the carbides led to a large drop in the microhardness. Although the chemical composition of cast IN617B alloy does not change compared with wrought IN617B alloy, different processing methods will lead to different mechanical properties and microstructures. Due to the lack of detailed microstructural data of cast IN617B alloy, it makes the investigation necessary and novel. This research characterized phase precipitation and tensile properties of cast IN617B alloy during solution heat treatment and long-term aging treatment and predicted the phase stability of cast IN617B alloy during long-term thermal exposure at a service temperature of 700 °C. At last, the objective of this investigation is to provide necessary data for the application of cast IN617B alloy.

2 Experimental

Table 1 shows the nominal composition of the investigated alloy. Experimental alloy was melted in an industrial scale vacuum induction furnace and then cast into the rods with 15 mm in diameter and 220 mm in length. The as-cast rods used for long-term thermal exposure were subjected to solution heat treatment at 1200 °C for 2 h followed by water cooling (WC). Subsequently, the alloy was subjected to long-term aging treatment at 700 °C for 100, 300, 500, 1000, 3000 and 5000 h, respectively. Observation of the microstructural evolution of each specimen was conducted by scanning electron microscope (SEM) equipped with energy dispersive spectrometer (EDS), electron probe microanalysis (EMPA), transmission electron microscope (TEM) and high resolution TEM. Before SEM and EPMA observations, the surfaces of all samples were polished and then electrolytically etched at room temperature for 30−60 s at 15 V. Electrolytic etching which stripped away the γ-matrix, was employed for three-dimension observation of precipitates with an electrolyte containing 300 mL HCl + 100 mL HNO_3 + 500 mL C_2H_5OH. Specimens for TEM observation were mechanically ground to 50 μm and then thinned by twin-jet electro-polishing with a solution of 10 mL $HClO_4$ + 90 mL C_2H_5OH at 20 V and −50 °C. The statistical data of precipitates (γ' diameter and area fraction, bar-like carbide length) were made mainly on TEM photographs of the particles. More than ten photographs with more than 100 precipitated particles were measured to minimize the experimental errors and the average value was taken as the statistical value.

Table 1 Nominal composition of alloy (mass fraction, %)

C	Cr	Co	Mo	Al	Ti	B	Ni
0.04	22	12	8	1.2	0.4	0.004	Bal.

High temperature tensile tests were conducted using an applied strain rate of 1×10^{-4} s^{-1} at 700 °C. Smooth cylindrical specimens had an overall length of 70 mm with gauge length and diameter of 25 and 5 mm, respectively. Moreover, TEM analysis was performed on material taken in the horizontal orientation from the gage length of tensile specimens in order to investigate the influence of the precipitates on deformation behavior. The thermodynamic calculation of the equilibrium microstructures, phases and precipitation kinetics was performed using JMatPro Version 7.0 with the Ni-based alloy database.

3 Results

3.1 Phase calculation

In order to predict the possible phases in the long-term aging microstructure of the alloy, thermo-dynamic calculation was performed using the software JMatPro 7.0 with Ni-based alloy database. The temperature-dependent equilibrium phase fraction is shown in Fig. 1. It can be found that the types of the

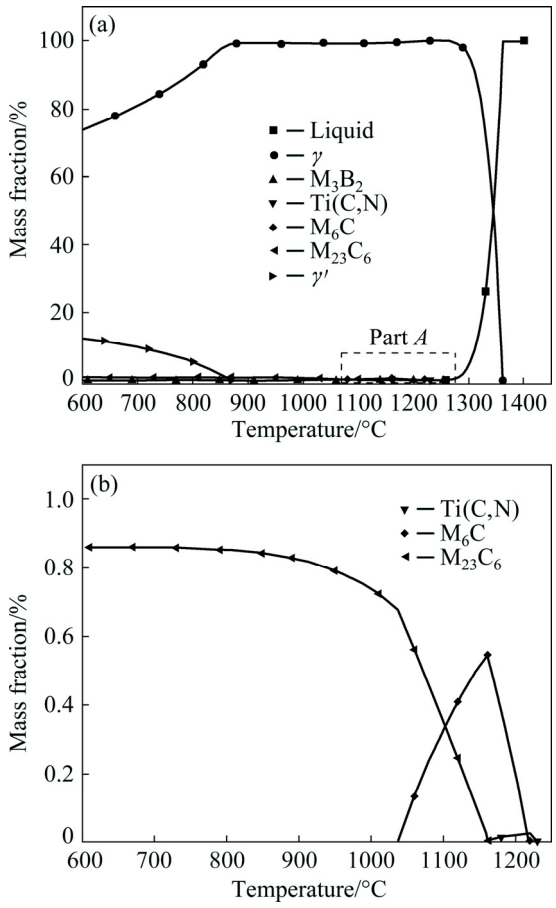

Fig. 1 Calculated temperature-dependent equilibrium phase fractions in IN617B alloy: (a) Whole equilibrium phase diagram; (b) Magnified diagram of part *A* in (a)

predicted phases consist of γ, γ', M_3B_2, Ti(C,N), M_6C and $M_{23}C_6$ under equilibrium condition. The amount of M_3B_2 and Ti(C,N) is relatively low in the alloy. And it is determined that the main phases are γ, γ' and $M_{23}C_6$ in the equilibrium microstructure at 700 °C (Fig. 1(a)). In addition, it is found that the amount of primary carbides ($M_{23}C_6$ and M_6C) decreases at the temperature over 1200 °C as shown in Fig. 1(b). This suggests that coarse phases will be dissolved into the matrix after heat treatment of 1200 °C, contributing to enhancing the solution strengthening. Therefore, we decide to select the temperature of 1200 °C as the solution annealing temperature of the alloy. In addition, the solution annealing time of 2 h is long enough to eliminate element segregation and dissolve primary carbides in as-cast microstructures, which is confirmed by the additional experiments.

3.2 Microstructure before long-term aging

The SEM images in Fig. 2 reveal that the as-cast alloy has an obvious dendritic segregation pattern with the average secondary dendrite arm space of 77.3 μm. The as-cast microstructure consists of the γ-matrix and a small amount of carbides. And these carbides mainly distribute in interdendritic regions. As the three-dimension morphologies are shown in Figs. 2(b) and (c), GBs and precipitates are surrounded by a deep gap which is the result of the deep etching. The GBs are decorated with strip-like or blocky particles, as shown in Fig. 2(b). The type of precipitates is confirmed by EDS analyses (Table 2) where C element is excluded for percent calculation. This indicates that the strip-like carbides are Cr-rich $M_{23}C_6$ and the blocky carbides are Mo-rich M_6C. In backscattered scanning electron microscopy (BSEM) images, there are some blocky carbides with dark

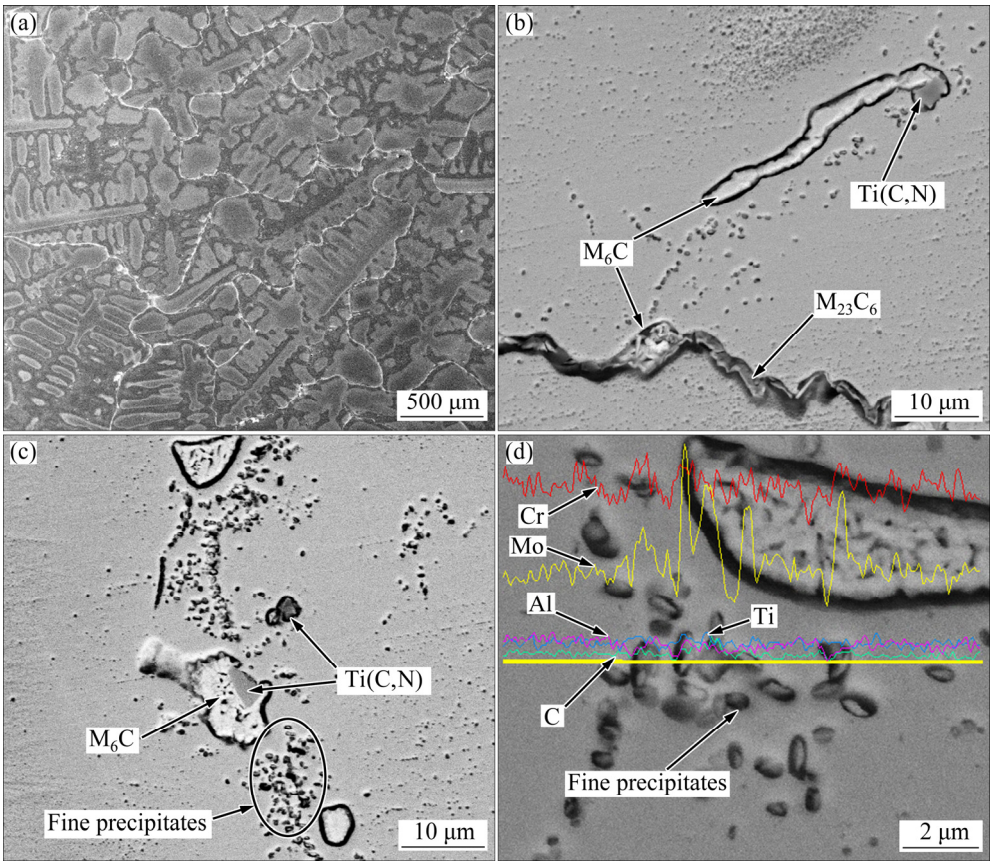

Fig. 2 Microstructures of as-cast alloy: (a) SEM image of dendritic microstructure; (b, c) BSEM images showing inter- and intra-granular carbides; (d) Magnified SEM line scan result of fine precipitates

Table 2 EDS analysis of carbides with different morphologies

Carbide	Morphology	Mass fraction/%						Mole fraction/%					
		Al	Ti	Cr	Co	Ni	Mo	Al	Ti	Cr	Co	Ni	Mo
Ti(C,N)	Dark and blocky	3.81	72.2	5.15	2.04	4.82	11.32	7.1	75.84	4.98	1.74	4.13	6.02
M_6C	Blocky	0.01	1.32	25.35	2.01	5.42	67.15	0.03	2.06	39.63	2.55	6.88	52.67
$M_{23}C_6$	Strip-like	0.37	0.21	38.89	7.49	32.56	21.91	0.83	0.26	45.06	7.66	33.41	13.84

contrast which are determined to be Ti-rich Ti(C,N) according to Table 2. Within grains, gray contrast and blocky carbides are confirmed as Mo-rich M_6C according to EDS analyses. In addition, Figs. 2(b) and (c) show that M_6C and Ti(C,N) tend to co-exist easily. Lots of fine particles distribute around blocky carbides, as marked in Fig. 2(c). As revealed by the EDS line scan in Fig. 2(d), these fine precipitates are Mo-rich M_6C with the high peak of Mo. According to the statistical data of SEM images, it is found that the average size of blocky carbides is about 11 μm and the area fraction is 0.9%.

Figures 3(a) and (b) show the microstructure morphologies after solution heat treatment at 1200 °C for 2 h followed by WC. In Fig. 3(a), it is very hard to distinguish dendrite patterns and coarse carbides, which indicates that composition segregation is eliminated and most of carbides are dissolved into the matrix. But a small number of fine and black particles exist within grains. And these particles are determined as Ti(C,N) by the corresponding EDS result in Fig. 3(a′), which is the result of the incomplete dissolution of primary Ti(C,N) during solution annealing. In addition to Ti(C,N) particles, GBs still are decorated with film-shape carbides as shown in Fig. 3(b). The film-shape carbides are confirmed as Cr-rich $M_{23}C_6$ precipitating directly during cooling from high temperature according to the corresponding EDS result Fig. 3(b′). Compared with microstructure of the as-cast alloy, an obvious distinction is that a deep gap disappears near GBs and precipitates in solution-treated microstructure subjected to the same electrolytic etching. This is largely ascribed to the dissolution of primary carbides which releases lots of Cr element into the matrix, contributing to the improvement of the corrosion resistance of the matrix near GBs. This is similar to results in Ref. [15] related to alloy 690. The formation of carbides at GBs led to the Cr-depletion zone near GBs in the microstructures of as-cast alloy. As seen in the above SEM observation (Figs. 2 and 3), depleted-Cr matrix in the microstructure of as-cast alloy is easily eroded by a deep etching method while the phenomenon is not observed in the solution-treated microstructure.

3.3 Long-term aging microstructure

After long-term aging at 700 °C for different time, the phase precipitation of the experimental alloy is revealed in Fig. 4. It is clearly seen that the morphology of GB carbides remarkably changes with the increase of aging time. After aging for 100 h, the morphology of GB carbides remains film-shape, which is the same as that of the solution-treated microstructure (Fig. 4(a)). But after aging for 300 h, GB carbides appear as an irregular and

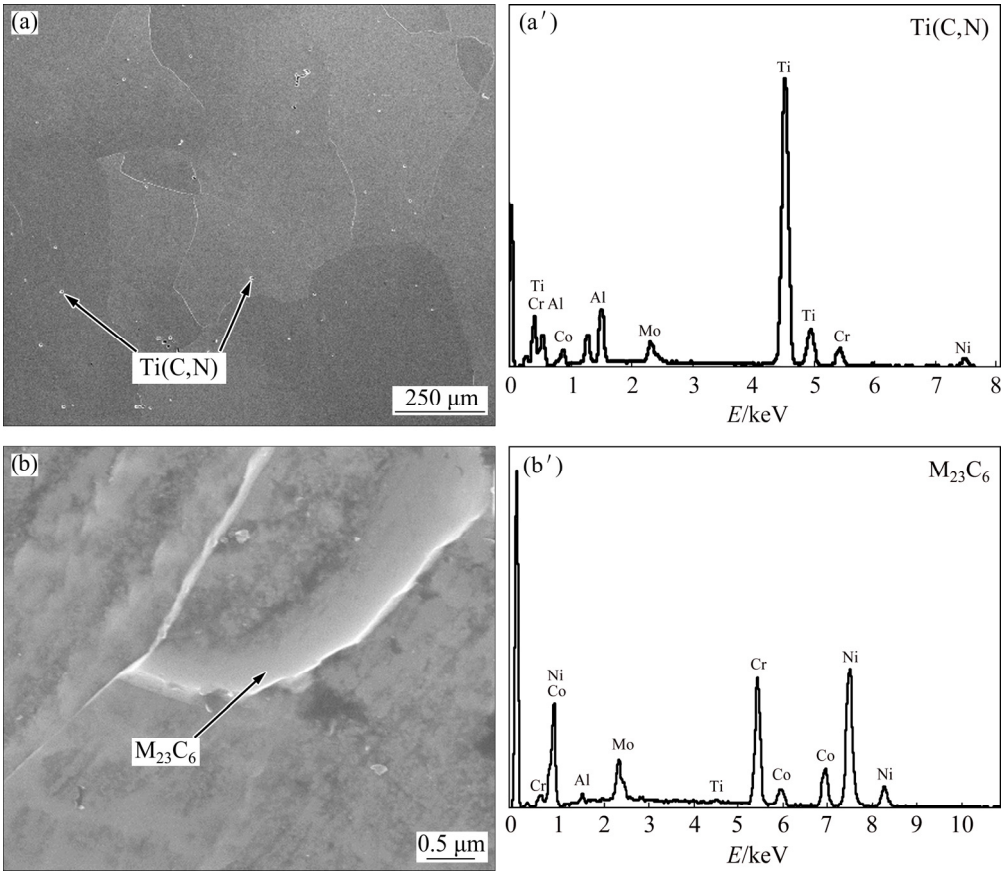

Fig. 3 Microstructure (a) of solution-treated alloy showing fine Ti(C,N) particles with corresponding EDS (a′) and that (b) showing film-shape carbides at GBs with corresponding EDS (b′)

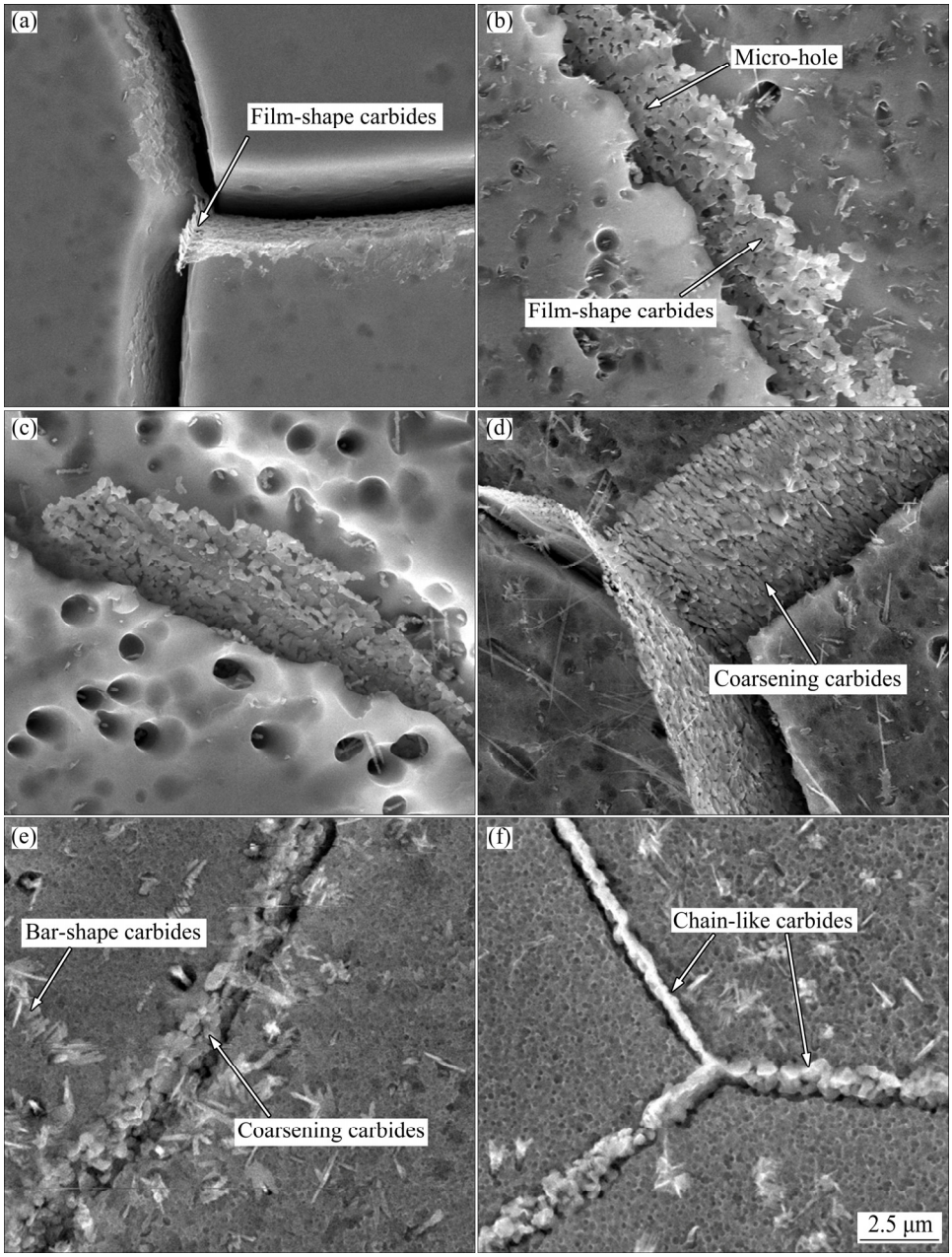

Fig. 4 Microstructures after aging at 700 °C for 100 h (a), 300 h (b), 500 h (c), 1000 h (d), 3000 h (e) and 5000 h (f)

film-like morphology, as shown in Fig. 4(b). In the period of 500−1000 h (Figs. 4(c) and (d)), chip-like GB carbides become denser and smaller than those in the microstructure after aging for 300 h. Subsequently, chip-like GB carbides coarsen distinctly and transform into cellular GB carbides (Fig. 4(e)) during aging for 3000 h. After aging of 5000 h, plenty of cellular GB carbides crowd at GBs and even combine with each other, resulting in the coarsening of GB carbides which are considered to be detrimental to the mechanical properties of alloys (Fig. 4(f)). Simultaneously, the transformation of GB carbides is accompanied by the diffusion of alloying elements, which is demonstrated by EPMA observations. Figure 5 shows an EPMA elemental distribution map of the microstructure after aging for 500 h, which reveals that C and Cr remarkably segregate to GBs. Notice that GB carbides are rich in Cr and poor in Mo, and blocky carbides adjacent to GBs are rich in Ti. Therefore, it is deduced that GB carbides are Cr-rich $M_{23}C_6$. Blocky particles near GBs are determined to be Ti(C,N) type carbides according to EPMA result. In addition, the main phases within grains are short and bar-shape carbides which directly precipitate in the matrix, as revealed in Fig. 4. Based on TEM observation (Fig. 6), they are determined to be $M_{23}C_6$ carbides. These carbides gradually coarsen with increasing aging time.

Figure 6 shows TEM morphology and selected area

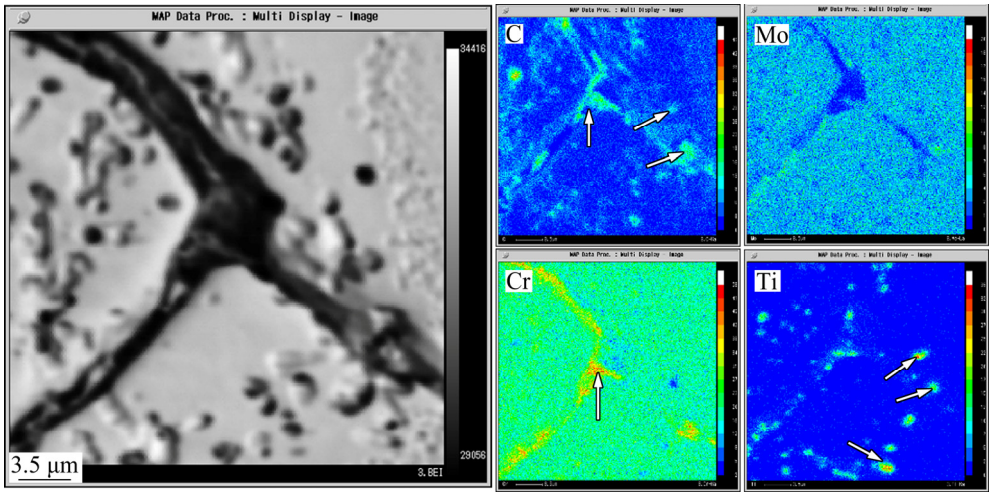

Fig. 5 Elemental distribution maps of GBs after aging for 500 h (element enrichment regions are marked by arrows)

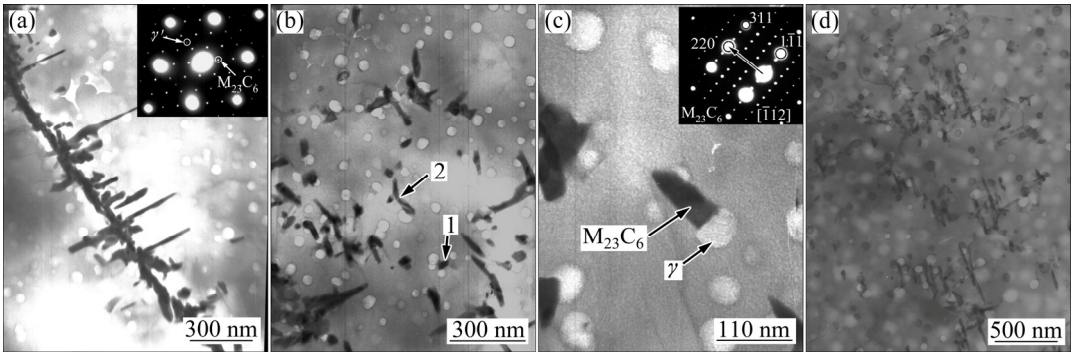

Fig. 6 TEM morphologies of carbides after aging for 500 h (a−c) and 5000 h (d): (a) Topography of GB carbides with corresponding SAD pattern at top-right corner; (b) Topography of GB carbides and γ' within grains; (c) TEM topography showing inhibiting effect of γ' on coarsening of $M_{23}C_6$; (d) TEM topography showing microstructure after aging for 5000 h

diffraction (SAD) pattern of carbides and γ' after aging for 500 and 5000 h, respectively. Figure 6(a) reveals that $M_{23}C_6$ carbides grow into grains from GBs, meanwhile, a large amount of $M_{23}C_6$ and γ' appear within grains. It is found that γ' has influence on the topography of $M_{23}C_6$ as marked by arrows 1 and 2 in Fig. 6(b). At arrow 1, $M_{23}C_6$ appears as a granular shape, and at arrow 2, bar-like $M_{23}C_6$ has a curved surface. Bar-like $M_{23}C_6$ generally grows up along one crystallographic orientation, but the growth comes to the end in front of γ', as shown in Fig. 6(c). The corresponding SAD of bar-like $M_{23}C_6$ (the right-top inset in Fig. 6(c)) shows that the bar-like carbides grow along the [110] direction which is parallel to the lattice plane indices (220) in SAD. In addition, it also reveals that the cube-on-cube coherent orientation relationship between $M_{23}C_6$ and the matrix γ is as follows: $(1\bar{1}1)_{M_{23}C_6}//(1\bar{1}1)_{\gamma}$. According to the SAD in the [011] zone axis, it is confirmed that $M_{23}C_6$ carbide has a FCC crystal structure with a lattice parameter of a=1.03 nm which is consistent with the results in Refs. [16,17]. Figure 6(d) shows that the main precipitates are $M_{23}C_6$ carbides and γ' phase after aging for 5000 h and they keep small size and distribute uniformly in the microstructure. In addition, according to the statistical data of TEM images (Table 3), the average size of circular γ' increases from 34.3 to 55.1 nm and the area fraction increases from 11.1% to 15.0%. And the length of bar-like $M_{23}C_6$ rises from 89.3 to 125.0 nm. During long-term thermal aging, the serious coarsening behavior of carbides and the precipitation of detrimental TCP phase are not observed.

Table 3 Statistical data of precipitates after aging for 500, 3000 and 5000 h

Aging time/h	Diameter for circular γ'/nm	Area fraction for circular γ'/%	Length for bar-like $M_{23}C_6$/nm
500	34.3±7.1	11.1±0.04	89.3±50.1
3000	49.2±5.3	14.5±0.03	110.2±28.2
5000	55.1±14.5	15.0±0.01	125.0±37.3

3.4 Tensile properties and deformation microstructures

Tensile properties of the experimental alloy at 700 °C after standard heat treatment and aging for 5000 h are shown in Fig. 7. The tensile strength at

700 °C including the yield strength ($\sigma_{0.2}$) and the ultimate tensile strength (σ_b) increases obviously after long-term aging, meanwhile the tensile strength at 700 °C after aging for 3000 h is nearly the same as that after aging for 5000 h (Fig. 7(a)). However, the ductility including the elongation (δ) and the reduction area (φ) decreases by nearly two times (Fig. 7(b)). Representative TEM micrographs from the 5000 h aged specimen subjected to tensile test at 700 °C are shown in Fig. 8. It is revealed that the dislocation density remains fairly high and dislocations interact strongly with the γ' particles and carbides. It is clear that a large amount of dislocations align themselves into regular array and walls (Fig. 8(a)). Moreover, it is observed that lots of dislocations are pinned surround carbides, as shown in Fig. 8(b). Two kinds of interactions between dislocations and γ' particles, Orowan looping (black arrows) and local dislocation climbing (white arrows), are evident in Fig. 8(c). These indicate that the deformation mechanism of the alloy at 700 °C is mainly dominated by dislocation gliding and climbing, but the former holds a leading position.

4 Discussion

4.1 Evolution of carbides at GBs

According to the SEM observation of the as-cast microstructure (Fig. 2), the phases consist of γ, Ti(C,N), M_6C and $M_{23}C_6$, which is almost in consistent with phase calculation results. In addition, carbides mainly distribute in interdendritic regions due to the segregation of Mo and Cr elements. These refractory and heavy elements tend to segregate into interdendritic regions during alloy solidification. This contributes to the formation of Cr-rich $M_{23}C_6$ and Mo-rich M_6C in interdendritic regions. Subsequently, element segregation is eliminated and large carbides almost completely dissolve after the solution heat treatment at 1200 °C for 2 h. Based on the observation (Fig. 3), an incomplete solid−solution occurs in the alloy with a small amount of fine Ti(C,N) particles and second film-shape carbides. Generally, Ti(C,N) particles are common nitride−carbides in nickel-based superalloys, which possesses a relatively stable structure. It is hard to dissolve Ti(C,N) into the matrix during high temperature solution heat treatment [11,18].

During the long-term aging, GB carbides gradually coarsen with increasing the aging time, as shown in Fig. 4. The present authors attempt to explain the transformation of carbides at GBs by a proposal schematic diagram (Fig. 9). This transformation process is divided into two states: the metastable stage and the growing stage. Firstly, the morphology of GB carbides keeps unbroken and film-like shape after aging for 100 h (Fig. 4(a)). But at high temperature, film-shape phase is

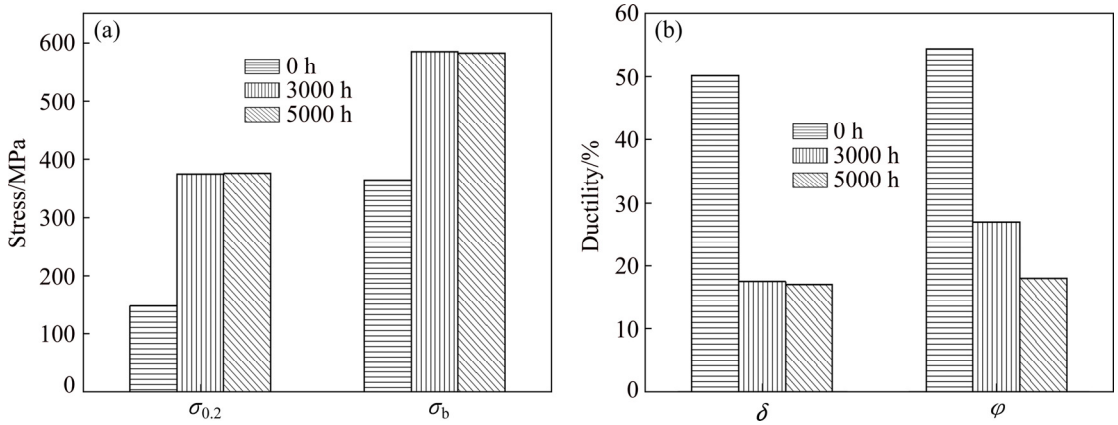

Fig. 7 Tensile properties of experimental alloy at 700 °C after standard heat treatment and aging for 5000 h: (a) Tensile strength and yield strength; (b) Elongation and reduction area

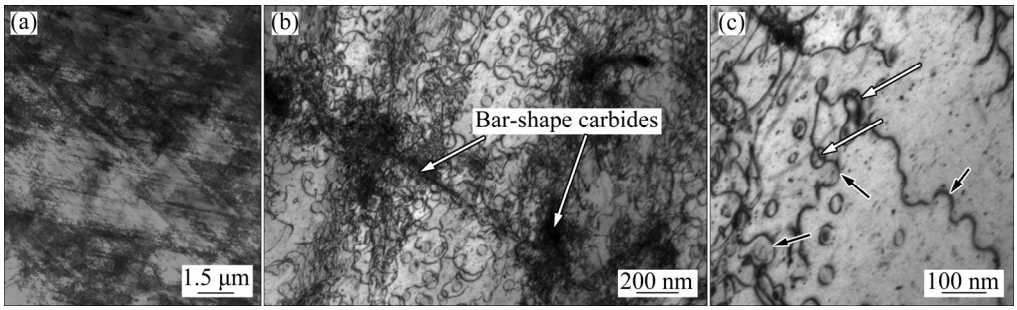

Fig. 8 TEM micrographs of specimen aged for 5000 h and subjected to tensile test at 700 °C: (a) Deforming microstructure; (b, c) Dislocation interaction with carbides and γ' particles (black arrows identify dislocation loop; white arrows indicate local dislocation climbing)

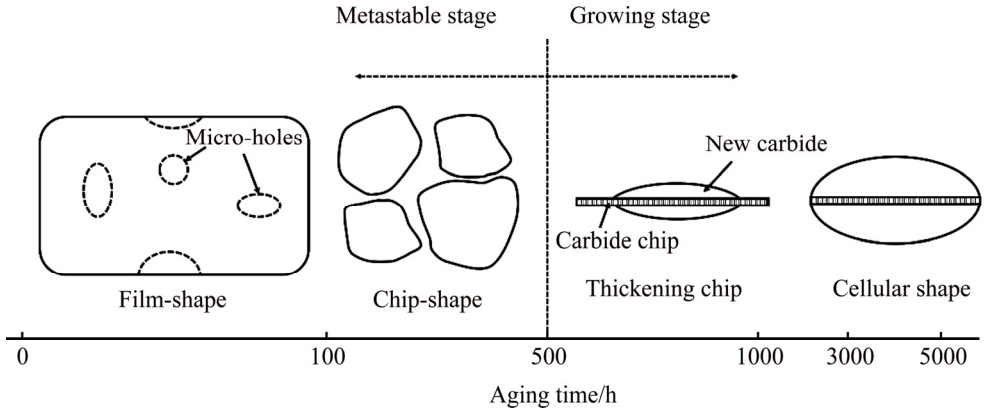

Fig. 9 Schematic illustration of transformation of GB carbide morphology

the unstable structure with a high surface energy. When a small perturbation impacts on the phase surface, some ruptures or micro-holes are induced on the phase surface [19]. It is ascribed to that the unbalance of concentration field at the perturbed point results in the dissolution of local phase. With the increase of aging time, a lot of micro-holes expand and connect with each other, leading to the fracture of primary GB carbide film (Fig. 4(b)). Therefore, these carbides become smaller and denser chips with a low surface energy after aging for 300 and 500 h. This indicates that the reduction in the surface energy is responsible for the morphological transition. But, after aging for 1000 h, Fig. 4(d) clearly reveals the evidence of the remarkable increase of chip-like carbide thickness. This is mainly ascribed to the fact that large amount of C and Cr elements strongly segregate to the GBs (Fig. 5) during the aging. The driving force for the precipitation of carbide at GBs is expected to be strikingly enhanced. As a result, these chip-like carbides have transformed into cellular carbides filling in GBs after longer aging for 3000 h, as shown in Fig. 4(e). Subsequently, every cellular carbide at GBs tends to aggregate gradually and even form a wide and continuous carbide chain after long-term aging for 5000 h (Fig. 4(f)). The kind of chain-like carbides is detrimental to mechanical properties of alloys, which is verified by lots of studies at GB carbides in Ni-based superalloys [8,9,20,21], because it will weaken the binding force of GB and damage the integrality of matrix. The formation of coarse and chain-like carbides at GBs should be avoided as much as possible in material design. In this work, the authors will try the best to eliminate the harmful phenomenon with some methods in the future.

4.2 Evolution of carbides within grains

As observed by SEM and TEM, second $M_{23}C_6$ carbides with a bar-like shape distribute mainly on both sides of GBs during the aging. This attributes to that primary $M_{23}C_6$ and M_6C carbides at GBs dissolve into the nearby matrix during solution heat treatment, and then provide atom C for the formation of secondary carbides. The bar-like $M_{23}C_6$ carbides grow along a preferential growth direction [110], as shown in Fig. 6(d). The observation is consistent with the results of previous studies [22] reporting that $M_{23}C_6$ particles grow along the ⟨110⟩ directions on {111} planes. This is ascribed to that the good matching crystallographic direction between the matrix and $M_{23}C_6$ is the ⟨110⟩ direction on {111} plane. Besides, it is noteworthy that the growth of bar-shape $M_{23}C_6$ is impeded by γ' particles when γ' particles encounter $M_{23}C_6$. When γ' particles nucleate near carbides, the barrier, which constrains the diffusion of Cr and Mo, forms around carbides. This results in inhibiting the aggregation of carbide formation elements. The inhibiting effects of γ' on the coarsening of $M_{23}C_6$ are divided into two cases. For one thing, when γ' precipitates distribute on both sides of bar-shape $M_{23}C_6$, they prevent the coarsening of $M_{23}C_6$ carbides perpendicular to the [110] direction, giving rise to a curving shape of the particles, as marked by arrow 2 in Fig. 6(b). For the other thing, as γ' particles distribute on the growth [110] direction, they hinder the growth of $M_{23}C_6$ carbides parallel to the [110] direction, resulting in a granular shape of carbides, as marked by arrow 1 in Fig. 6(b). For the alloy, the inhibiting effect on the coarsening of $M_{23}C_6$ is beneficial to the microstructural stability. Such stable carbides and dispersed γ' particles are conducive to the elevated temperature creep resistance of alloys. This is ascribed to that dispersed second-phase can hinder the motion of dislocations and delay the accumulation of dislocations at GBs. As a result, it puts off the concentration of stress and the initiation of microcracks [11]. These beneficial characteristics imply that the as-cast alloy has a relatively stable microstructure during long-term aging at 700 °C.

4.3 Effects of precipitates on tensile properties of experimental alloy at 700 °C

According to tensile properties (Fig. 7), the tensile strength of the aging alloy at 700 °C increases obviously while the ductility decreases distinctly compared with that of solution treated specimen. This is mainly ascribed to the precipitate strengthening of γ' phase and carbides which have strong hindering effects on dislocation motion. This strengthening mechanism is explained by Orowan bowing mechanism as follows:

$$\tau=Gb/(L-2r) \quad (1)$$

where τ is the flow stress of which dislocation motion needs, G is the shear modulus, b is the Burgers vector value of the dislocations, $(L-2r)$ is the effective distance between obstacles. According to the statistical data (Table 3), the size and area fraction of γ' in the alloys aged for 3000 and 5000 h are close. Therefore, an invariable effective distance $(L-2r)$ can be expected. At the beginning of aging, the precipitation of γ' is a rapid process due to supersaturated microstructure [14]. But, the continuous precipitation of γ' is a relatively slow process during long-term aging because the as-cast IN617B alloy contains limited amount of γ' formation elements (Al and Ti). The time interval between 3000 and 5000 h is too short to form γ' by slow element diffusion. This is also the reason why γ' particles do not ripen obviously. In addition, it is found that the size of $M_{23}C_6$ precipitates has no obvious change. As a result, the flow stress τ is not influenced by $M_{23}C_6$ precipitates after aging for 5000 h. This is ascribed to the inhibiting effect of γ' on the coarsening of $M_{23}C_6$ as mentioned in the previous microstructure analysis. Besides, it is planed that the microstructure observation after longer time aging will be carried out in the future.

In addition, it is observed that the plasticity of the alloy remarkably decreases after long-term aging compared with that after solution heat treatment. This is primarily attributed to that the precipitation of γ' phase and carbides provides a strong resistance to the movement of dislocations. During tensile deformation, the increase of loading stress activates two deformation mechanisms: Orowan bowing and dislocation climbing around the γ' phase, as shown in Fig. 8(c). Therefore, this shows that the long-term aging caused considerable degradation in the plasticity of the experimental alloy.

5 Conclusions

1) Ti(C,N), M_6C and $M_{23}C_6$ were the primary precipitates in the as-cast microstructure. Most of primary carbides dissolved into the matrix after solution heat treatment.

2) During long-term aging at 700 °C, the morphology of GB carbides evolved from film-like shape to chip-like shape and finally to cellular shape with the increase of aging time on account of the reduction in the surface energy and the segregation of the formation elements into GBs.

3) The $M_{23}C_6$ carbides with a bar-like morphology preferentially grew along the [110] direction within grains. The coarsening of $M_{23}C_6$ was strongly inhibited by γ' particles through constraining the diffusion of formation elements.

4) The tensile strength of the alloy obviously increased, but the ductility significantly decreased after aging for 5000 h, because the precipitation of γ' particles and carbides strongly blocked the mobile dislocations. Two deformation mechanisms: Orowan bowing and dislocations climbing were activated.

References

[1] JABLONSKI P D, HAWK J A, COWEN C J, MAZIASZ P J. Processing of advanced cast alloys for A-USC steam turbine applications [J]. JOM, 2012, 64(2): 271–279.

[2] VISWANATHAN R, HENRY J F, TANZOSH J, STANKO G, SHINGLEDECKER J, VITALIS B, PURGERT R. U.S. program on materials technology for ultra-supercritical coal power plants [J]. Journal of Materials Engineering and Performance, 2013, 22(10): 2904–2915.

[3] SUN F, GU Y F, YAN J B, ZHONG Z H, YUYAMA M. Tensile deformation-induced dislocation configurations at intermediate temperatures in a Ni−Fe-based superalloy for advanced ultra-supercritical coal-fired power plants [J]. Journal of Alloys and Compounds, 2016, 657(4): 565–569.

[4] LIU Li-rong, JIN Tao, LIU Jin-lai, SUN Xiao-feng, HU Zhuang-qi. Effect of ruthenium on γ' precipitation behavior and evolution in single crystal superalloys [J]. Transactions of Nonferrous Metals Society of China, 2013, 23(1): 14–22.

[5] JAHANGIRI M R, ARABI H, BOUTORABI S M A. Comparison of microstructural stability of IN939 superalloy with two different manufacturing routes during long-time aging [J]. Transactions of Nonferrous Metals Society of China, 2014, 24(6): 1717–1729.

[6] GUO Yan, ZHANG Zhou-bo, ZHOU Rong-ban, HOU Shu-fang, WANG Bo-han. Microstructure and mechanical properties of alloy 617B [J]. Transactions of Nonferrous Metals Society of China, 2015, 25(4): 1106–1113.

[7] KLÖWER J, HUSEMANN R U, BADER M. Development of nickel alloys based on alloy 617 for components in 700 °C power plants [J]. Procedia Engineering, 2013, 55(11): 226–231.

[8] DI M S F, FAULKNER R G, HOGG S C, VUJIC S, TASSA O. Characterisation of microstructure and creep properties of alloy 617 for high-temperature applications [J]. Materials Science and Engineering A, 2014, 619(3): 77–86.

[9] RAHMAN M S, PRIYADARSHAN G, RAJA K S, NESBITT C, MISRA M. Characterization of high temperature deformation behavior of Inconel 617 [J]. Mechanics of Materials, 2009, 41(3): 261–270.

[10] HOLCOMB G R, JABLONSKI P D, WANG P. Cast alloys for advanced ultra supercritical steam turbines [C]//Proc Superalloys 2010. Warrendale, PA: TMS, 2010: 946–960.

[11] TYTKO D, CHOI P P, KLÖWER J, KOSTKA A, INDEN G, RAABE D. Microstructural evolution of a Ni-based superalloy (617B) at 700 °C studied by electron microscopy and atom probe

tomography [J]. Acta Materialia, 2012, 60(4): 1731–1740.
[12] MANKINS W L, HOSIER J C, BASSFORD T H. Microstructure and phase stability of Inconel alloy 617 [J]. Metallurgical Transactions, 1973, 5(12): 2579–2590.
[13] KIHARA S, NEWKIRK J B, OHTOMO A, SAIGA Y. Morphological changes of carbides during creep and their effects on the creep properties of Inconel 617 at 1000 °C [J]. Metallurgical Transactions A, 1978, 11(6): 1019–1031.
[14] WU Q, SONG H, SWINDEMAN R W, SHINGLEDECKER J P, VASUDEVAN V K. Microstructure of long-term aged IN617Ni-base superalloy [J]. Metallurgical and Materials Transactions A, 2008, 39(11): 2569–2585.
[15] LI Hui, XIA Shuang, ZHOU Bang-xin, PENG Jian-chao. Study of carbide precipitation at grain boundary in nickel base alloy 690 [J]. Acta Metallurgica Sinica, 2011, 47(7): 853–858.
[16] HONG H U, RHO B S, NAM S W. Correlation of the $M_{23}C_6$ precipitation morphology with grain boundary characteristics in austenitic stainless steel [J]. Materials Science and Engineering A, 2001, 318(1–2): 285–292.
[17] JO T S, LIM J H, DO K Y. Dissociation of Cr-rich $M_{23}C_6$ carbide in alloy 617 by severe plastic deformation [J]. Journal of Nuclear Materials, 2010, 406(3): 360–364.
[18] XU S, DICKSON J I, KOUL A K. Grain growth and carbide precipitation in superalloy, UDIMET 520 [J]. Metallurgical and Materials Transactions A, 1998, 29(11): 2687–2695.
[19] QIN Xue-zhi, GUO Jian-ting, YUAN Chao, HOU Jie-shan, YE Heng-qiang. Precipitation and thermal instability of $M_{23}C_6$ carbide in cast Ni-base superalloy K452 [J]. Materials Letters, 2008, 62(2): 258–261.
[20] CABIBBO M, GARIBOLDI E, SPIGARELLI S, RIPAMONTI D. Creep behavior of Incoloy alloy 617 [J]. Journal of Materials Science, 2007, 43(8): 2912–2921.
[21] KIM W G, YIN S N, LEE G G, KIM Y W, KIM S J. Creep oxidation behaviour and creep strength prediction for alloy 617 [J]. International Journal of Pressure Vessels and Piping, 2010, 87(6): 289–295.
[22] LEWIS M H, HATTERSLEY B. Precipitation of $M_{23}C_6$ in austenitic steels [J]. Acta Metallurgica, 1965, 13(11): 1159–1168.

一种铸造镍基高温合金在热处理过程中的相析出行为和拉伸性能

高 双[1,2]，侯介山[1]，郭永安[1]，周兰章[1]

1. 中国科学院 金属研究所，沈阳 110016；
2. 中国科学院大学，北京 100049

摘 要：研究一种铸造镍基合金(IN617B 合金)在固溶处理和长期时效处理过程中的相析出行为和拉伸性能。在铸态的组织中，Ti(C,N)、M_6C 和 $M_{23}C_6$ 为主要析出相，而经过固溶处理后，除少量 Ti(C,N)残余外，绝大部分碳化物固溶到基体中。在 700 °C 长期时效过程中，合金中相的析出行为主要包括 3 个方面：(1) 晶界处 $M_{23}C_6$ 碳化物的形貌由膜状转变成颗粒状，同时由于界面能的降低和元素向晶界的扩散，颗粒碳化物逐渐粗化；(2)晶内棒状 $M_{23}C_6$ 碳化物具有择优生长方向[110]，并与基体 γ 之间存在共格关系；(3) γ'颗粒可以通过限制碳化物形成元素的扩散来阻碍晶内 $M_{23}C_6$ 碳化物粗化。在时效 5000 h 后，合金的抗拉强度明显增加, 而合金的塑性明显下降。该合金具有稳定的显微组织，从而保证其在长期时效过程中具有优异的拉伸性能。

关键词：镍基高温合金；相析出；碳化物；γ'相；拉伸性能

(Edited by Wei-ping CHEN)